



n-Butane: Ignition delay measurements at high pressure and detailed chemical kinetic simulations

D. Healy^a, N.S. Donato^b, C.J. Aul^b, E.L. Petersen^b, C.M. Zinner^c, G. Bourque^d, H.J. Curran^{a,*}

^a Combustion Chemistry Centre, School of Chemistry, NUI Galway, Ireland

^b Department of Mechanical Engineering, Texas A&M University, College Station, TX, USA

^c Mechanical, Materials and Aerospace Engineering, University of Central Florida, Orlando, FL, USA

^d Rolls-Royce Canada Limited, 9500 Côte de Liesse, Lachine, Québec, H8T 1A2 Canada

ARTICLE INFO

Article history:

Received 28 September 2009

Received in revised form 2 January 2010

Accepted 19 January 2010

Available online 24 February 2010

Keywords:

n-Butane

Modeling

Ignition delay

Shock tube

Rapid compression machine

High pressure

Chemical kinetics

ABSTRACT

Ignition delay time measurements were recorded at equivalence ratios of 0.3, 0.5, 1, and 2 for *n*-butane at pressures of approximately 1, 10, 20, 30 and 45 atm at temperatures from 690 to 1430 K in both a rapid compression machine and in a shock tube. A detailed chemical kinetic model consisting of 1328 reactions involving 230 species was constructed and used to validate the delay times. Moreover, this mechanism has been used to simulate previously published ignition delay times at atmospheric and higher pressure. Arrhenius-type ignition delay correlations were developed for temperatures greater than 1025 K which relate ignition delay time to temperature and concentration of the mixture. Furthermore, a detailed sensitivity analysis and a reaction pathway analysis were performed to give further insight to the chemistry at various conditions. When compared to existing data from the literature, the model performs quite well, and in several instances the conditions of earlier experiments were duplicated in the laboratory with overall good agreement. To the authors' knowledge, the present paper presents the most comprehensive set of ignition delay time experiments and kinetic model validation for *n*-butane oxidation in air.

© 2010 The Combustion Institute. Published by Elsevier Inc. All rights reserved.

1. Introduction

Understanding the combustion chemistry of butane is of interest for practical applications and also because of its importance to the oxidation of higher-order hydrocarbons. For example, fuel-flexible gas turbines are in high demand in the power generation industry. While butane may not be a candidate fuel for use on its own, significant amounts of C₄H₁₀ show up in liquefied natural gas (LNG). Thus it is necessary to fully understand the combustion chemistry to avoid problems in the combustion system of engines such as flashback, blow off, instabilities, and autoignition [1,2]. In the development and performance of homogeneous charge compression ignition (HCCI) engines too there is a need to perform experiments to validate the detailed chemistry mechanisms for various higher-order hydrocarbons. We have recently published work on a blend comprised of 50% *n*-butane with 50% isobutane in air [3]. The focus of this paper is on the chemistry of *n*-butane fuel with another companion paper on isobutane ignition, and a comparison of both isomers of butane. The present work provides the validation of *n*-butane chemistry models at practical engine conditions.

Several studies have been conducted to explore the autoignition behavior of *n*-butane in an open vessel [4], in rapid compression machines (RCM) [5–11] and shock tubes [3,12–14], Table 1. Other studies on the oxidation of *n*-butane include static reactors [15–17], flow reactors [18–20], jet-stirred reactors [21–24], a motored engine [25], internal combustion engines [26,27], and homogeneous charge compression ignition engines [28,29].

Measurements in the RCM have been performed at temperatures between 600 and 900 K and pressures below 18 bar. In general, the results showed two-stage ignition and Negative Temperature Coefficient (NTC) behavior. Franck et al. [5] reported on the control of spontaneous ignition by studying the evolution of the spontaneous ignition of *n*-butane at varying heat dissipation rates. They found that, as the heat dissipation rate is enhanced, the minimum compressed gas temperature required for ignition is raised from 700 to 870 K at an approximate compressed-gas pressure of 15 atm. This increase was reported to be linked to the rate of cooling in the post compression period before significant chemical heat release begins to take place. Minetti et al. [6–8] studied the oxidation and autoignition of stoichiometric, lean ($\phi = 0.8$), and rich ($\phi = 1.2$) *n*-butane/air mixtures in the temperature range 700–900 K and at pressures of 9–11 bar. Information was obtained concerning cool flames and ignition delays. Product profiles for selected major and minor species were measured during a two-stage ignition process [7]. Kojima and Suzuoki [9] using an RCM, mea-

* Corresponding author.

E-mail address: henry.curran@nuigalway.ie (H.J. Curran).

URL: <http://c3.nuigalway.ie/> (H.J. Curran).

Table 1Summary of ignition delay data available for *n*-butane oxidation.

Author	Facility	<i>T</i> (K)	<i>P</i> (atm)	ϕ
Franck et al. [5]	RCM	600–900	≤18 bar	1.0
Minetti et al. [6–8]	RCM	700–900	9–11 bar	0.8–1.2
Kojima and Suzuoki [9,30]	RCM	700–850	≈30 bar	0.23–1.94
Griffiths et al. [10]	RCM	600–950	≤18 bar	1.0
Kim et al. [11]	RCM	720–900	16–18 bar	1.0
Burcat et al. [12]	ST	1242–1400	8.18–9.08	1.0
Horning et al. [13]	ST	1300–1700	1–6 atm	0.5–2.0

sured autoignition delays from lean to rich mixtures of butane/air under various speeds of swirl flow, and also performed photographic observation at 3000 frames per second. A lot of interesting features of the autoignition delay and the autoignition process were observed. Most notably, it was found that the swirl preferentially lengthens the autoignition delays of richer mixtures while lean mixtures with equivalence ratios less than about 0.6 were little affected. With the results of computer simulation, it was concluded that this preferential effect indicates that the adiabatic core, in which the autoignition chemistry proceeds adiabatically, breaks more easily in richer mixtures at higher swirl speeds. Although the detailed mechanism of this preferential breakdown could not be clarified, this and other features of the autoignition under the swirl were fully discussed and interpreted. Subsequently, Kojima [30] carried out a chemical modeling study of these data in addition to those recorded in a shock tube by Burcat et al. [12] in order to interpret these data more fully and test the ability of a number of detailed kinetic models to reproduce the ignition behavior.

Griffiths et al. [10] reported on the autoignition characteristics of *n*-butane, *n*-pentane, *n*-hexane, and *n*-heptane, and also isobutane, iso-octane, and toluene in stoichiometric mixtures with air following compression to temperatures in the range 600–950 K and pressures up to 9 bar. Emphasis was placed on the dependence of ignition delay on compressed-gas temperature, on the evolution of reaction as portrayed in the pressure-time records and on features of light output associated with single and two-stage ignition. They reported that *n*-butane behaved differently from its higher molecular weight counterparts. It was found to have a much lower reactivity compared to the larger *n*-alkanes and it was speculated that this may be associated with the failure to form di-peroxy species readily, the low-temperature chemistry being driven by the alkyl-peroxy radical isomerization and decomposition to oxygen products and OH radical.

Kim et al. [11] studied the effects of pressure and temperature on the autoignition of propane and *n*-butane blends using an RCM. The initial temperature and pressure of the compressed gas was varied in the range of 720–900 K and 16–18 bar, respectively, under stoichiometric conditions, $\phi = 1.0$. The results showed a two-stage ignition delay and NTC behavior which were the unique characteristics of the alkane series fuels. As the concentration of propane in the blend was increased from 20% to 40%, the autoignition delay time increased by between 41% and 55% at 750 K. Numerical reduced kinetic modeling was performed using the Shell model. Several rate coefficients were calibrated based on the experimental results to establish an autoignition model of the propane and *n*-butane blends.

Shock-tube ignition delay times were recorded by Burcat et al. [12] in a reflected-shock study of the alkanes from methane through pentane, for stoichiometric argon–simulated-air mixtures. With the exception of ethane, the ignition delay times decreased with increasing number of carbon atoms, though differences amongst the various fuels were not large. Horning et al. [13] measured ignition times for propane, *n*-butane, *n*-heptane, and *n*-dec-

ane behind reflected shock waves over the temperature range 1300–1700 K, and in the pressure range 1–6 atm. For *n*-butane, the test mixture composition varied from 3.25% to 13.0% O₂, at equivalence ratios of 0.5, 1.0 and 2.0. More recently, Ogura et al. [14] measured ignition delay times behind reflected shock waves for *n*-butane, isobutane and their mixtures at 1.0% fuel, at $\phi = 0.72$ diluted in argon at a pressure of approximately 2 atm.

Modeling studies of butane oxidation have been performed at both low- and high-temperature conditions [31,30,21,22,26,27,32–35]. Warnatz [31] published a general reaction mechanism to simulate lean and rich high-temperature combustion of hydrocarbons up to C₄-species. Pitz and Westbrook developed a model to simulate *n*-butane oxidation in a flow reactor and also used it to simulate ignition delay times and laminar flame calculations of flame speed and species profiles [19] and later simulated the oxidation of *n*-butane and its relation to engine knock [32] in addition to other engine studies [26,27,33]. Wang et al. [34] developed a reduced kinetic model to describe the autoignition of the butanes. Buda et al. published a paper on a unified detailed kinetic model for the autoignition of alkanes from C₄ to C₁₀ [35]. The compounds studied were *n*-butane, *n*-pentane, isopentane, neopentane, 2-methylpentane, *n*-heptane, iso-octane, *n*-decane, and mixtures of *n*-heptane and iso-octane. The conditions investigated were at temperatures in the range 600–1200 K, including the NTC region, pressures in the range 1–50 bar, and at equivalence ratios of 0.5–2.

In this current study, we detail a new comprehensive set of ignition delay time data over a wider range of equivalence ratio and pressure than previously reported and provide details of the chemical kinetic mechanism used to successfully simulate these new data. Provided below are brief descriptions of the rapid compression machine and shock-tube experiments, followed by a detailed discussion of the chemical kinetic model. The results of the current experiments are then presented, discussed, and compared with the new model. In addition, where possible we compare our data with those previously published in the literature, and overall there is reasonably good agreement.

2. Experimental

A common set of mixtures was selected for study in both the RCM and the shock tube. The mixture compositions are provided in Table 2. Some additional mixtures that overlapped with available results from the literature were also studied, the details of which are given later in the paper.

Some discussions of both the rapid compression machine [36–38] and the shock tube [39,40] have been provided previously, with a summary given in [41]. Provided in this section is a summary of the RCM facility followed by details on the shock-tube facilities, with emphasis on their application for the experiments herein.

2.1. Rapid compression machine

Butane gases were obtained from Aldrich at 99%+ purity, while all other gases were supplied by BOC Ireland; nitrogen (CP Grade) 99.95%, argon (Research Grade) 99.9995%, oxygen (Medical Grade) 99.5% and all were used without further purification. Test mixtures

Table 2*n*-Butane mixtures tested.

% <i>n</i> -C ₄ H ₁₀	O ₂	Diluent	ϕ
0.962	20.83	78.21	0.3
1.595	20.70	77.71	0.5
3.135	20.38	76.49	1.0
6.079	19.76	74.16	2.0

were prepared manometrically in a stainless steel container and allowed to mix thoroughly before use.

Measured pressure profiles are recorded using a pressure transducer (Kistler 603B) with the signal passing through a charge amplifier and saved on a digital oscilloscope. Experimental compression times are relatively short at approximately 16 ms. The ignition delay time, τ_{ign} , was defined as the time from the end of compression to the maximum rate of pressure rise; both events were reproducible to within 10% at each T_c . The composition of each mixture together with the experimental results and the initial conditions of charge composition, temperature and pressure are documented in Tables 1–12 of [Supplemental material](#). Even though ignition delays were observed up to 320 ms following compression, repeat experiments which had ignition delay times greater than 100 ms showed larger percentage variations in measured ignition delay times compared to those with ignition delay times below 100 ms, Tables 1–12 of [Supplemental material](#). Generally, we observe about a 5–10% variation in ignition delay times for repeat experiments.

The compressed-gas temperature, T_c , was calculated from the initial temperature, T_i , pressure, p_i , reactant composition, and the experimentally measured compressed-gas pressure, p_c . The compressed-gas pressure is defined as the maximum pressure immediately after compression. The temperature calculation employed the adiabatic compression/expansion routine in Gaseq [42] which uses the temperature dependence of the ratio of specific heats, γ , according to:

$$\ln\left(\frac{p_c}{p_i}\right) = \int_{T_i}^{T_c} \frac{\gamma}{\gamma - 1} \frac{dT}{T}$$

while assuming frozen chemistry during compression. Even though ignition delay times were observed up to 318 ms following compression ([Table 5, Supplemental material](#)), repeat experiments which had ignition delay times greater than 100 ms showed larger percentage variations compared to those with $\tau < 100$ ms.

[Fig. 1](#) presents a comparison of pressure versus time profiles for reactive and non-reactive (O_2 replaced by N_2) *n*-butane “air” mixtures, under stoichiometric conditions using nitrogen as the diluent at 10 atm. All mixtures show very similar pressure-time profiles after compression prior to cool-flame reactivity and second-stage ignition. This result is to be expected as the heat capacity and thermal conductivity of all mixtures are identical.

2.2. Shock tube

The shock-tube facilities utilized in this study are capable of obtaining the high temperatures and pressures required for this study. One-dimensional shock relations were used in conjunction

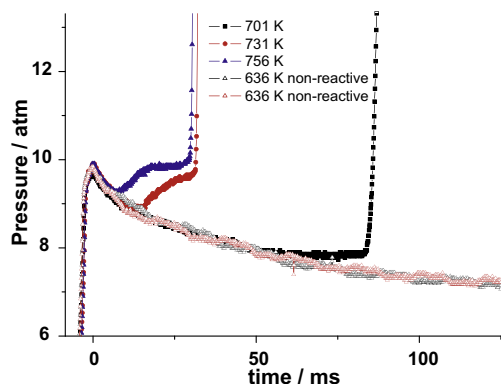


Fig. 1. Comparison of pressure versus time profiles for reactive and non-reactive *n*-butane/“air” mixtures, $\phi = 1.0$, $p_c = 10$ atm, taken in the RCM.

with the measured incident-shock velocity at the test region to determine the conditions behind the reflected shock. Both facilities use five pressure transducers (PCB 113) set up in series along the side of the shock tube to measure the incident-shock velocity. The pressure transducers feed signals to four Fluke PM 6666 timer counter boxes which are used to extrapolate the incident-shock velocity at the end wall. All experiments were performed by the reflected shock wave.

The first facility, discussed in detail by Aul et al. [43], has a circular driven section length of 4.72 m with an inner diameter of 15.24 cm, and a driver section length of 2.46 m with an inner diameter of 7.62 cm. This shock tube was utilized for the lower-pressure experiments and to obtain the 45-atm data. The other shock-tube facility, described in depth by Petersen et al. [40], was used to obtain the intermediate- to high-pressure data and has a driven section length and internal diameter of 10.7 m and 16.2 cm, respectively. The driver section has length and internal diameter of 3.5 m and 7.62 cm, respectively. Both shock-tube facilities are constructed entirely of stainless steel 304 and used helium as the driver gas. Pre-scored aluminum diaphragms were used to obtain the test conditions greater than about 5 atm, and polycarbonate diaphragms were used to obtain the 1-atm conditions.

Each shock tube is situated with PCB 134A and Kistler 603B1 pressure transducers at the sidewall and endwall locations to determine ignition delay time measurements from the highly exothermic pressure rise during ignition. Chemiluminescence emission measurements of OH^* are also made using a 307 ± 5 nm bandpass filter in sequence with a Hamamatsu 1P21 photomultiplier tube located at the sidewall and endwall locations through CaF_2 windows. All of the data signals are processed through a 14-bit GageScope digital oscilloscope with sampling rates of 1 MHz or greater per channel. The test mixtures were made in stainless steel mixing vessels using partial pressures to determine the volumetric percentage of each constituent to within 1% of their value. The N_2 and O_2 were premixed in the ratio of 3.76–1, and both were ultra high purity grade (99.9995%). The *n*-butane was obtained from Matheson for the experiments in the Petersen et al. [40] shock tube and from Praxair for the experiments on the Aul et al. [43] shock tube; both were of 99.95% purity.

Due to the exothermic nature of these reactions, ignition delay times, Tables 13–21 of [Supplemental material](#), were measured from the endwall as the sharp pressure rise seen after the reflected shock. This pressure rise coincides with the onset of OH^* emission which was used to qualitatively obtain ignition. However, both the pressure and OH^* emission measurements of ignition agreed within a few microseconds of each other and could have been used interchangeably to designate the final ignition delay times. This was because the real fuel/air mixtures utilized herein produced substantial energy release [44–46]. [Fig. 2](#) shows representative endwall pressure and OH^* emission traces used to determine ignition delay time.

As seen in [Fig. 2](#), which is representative of all the shock-tube data herein, there was no pre-ignition pressure rise due to anomalous early ignition events. Also, the pressure increase due to non-ideal facility effects such as boundary layer buildup was less than 2% per millisecond for every experiment, hence producing a minimal impact on the ignition results in the present paper, where most ignition delay times were below 1 ms. For example, at the conditions of [Fig. 2](#) (1148 K, 19.4 atm), a worst-case pressure rise of 2% per ms would result in a pressure at the time of ignition (due solely to boundary layer effects) of 19.64 atm; the corresponding temperature at 652 μs would then be 1152 K, or a 4-K increase over the time prior to ignition. Such a small increase in temperature would create a minimal impact on the ignition delay times reported herein and would be within the stated accuracy of the post-shock temperature. Approximately 50 μs before the igni-

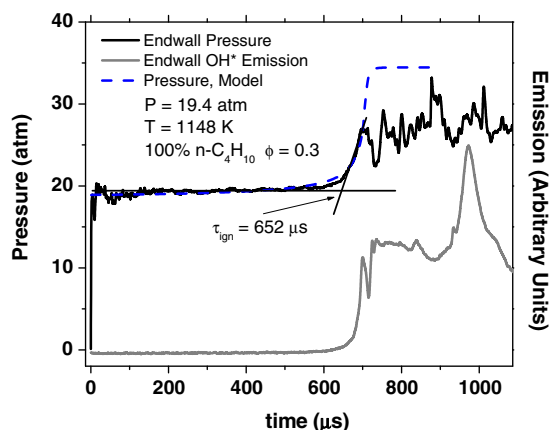


Fig. 2. Typical endwall pressure and emission traces used to determine ignition delay time for 100% *n*-butane at $T = 1148$ K, $\tau_{\text{ign}} = 652$ μs .

tion event in Fig. 2, there is an increase in pressure, but this increase can be shown to be due to the energy release during the adiabatic ignition process. Such an increase is not due to any facility effects and is predicted by the zero-dimensional chemical kinetics (discussed in more detail below) when modeling the shock-tube experiment as a constant-volume, constant-internal energy process. A sample calculation of the pressure is shown in Fig. 2, superimposed on the measured pressure trace.

As mentioned above, both argon and nitrogen were used in the RCM experiments, while in the shock-tube experiments only nitrogen was used as the diluent gas. The differences between them would be with respect to their impact on the heat transfer characteristics, which are addressed above for the RCM experiment. For relatively short ignition delay times seen in the shock-tube experiments, it is well known that heat loss to the tube walls is negligible, so that differences between argon and nitrogen on heat losses during a shock-tube experiment are non-existent. Any differences between nitrogen and argon with respect to the chemical kinetics were found to be minor, as shown in the presentation of the RCM data below. It has also been shown that for the high-fuel concentration and high-pressure conditions of the present experiments that the nitrogen (and oxygen) is vibrationally relaxed within the first several microseconds after passage of the reflected shock wave.

3. Model

The mechanism is based on the work of Curran et al. [47,48] and on our updated C_4 chemistry [49]. All rate constants for reaction types associated with C_4 chemistry are estimated in the same way as those detailed in the iso-octane paper [48], otherwise they are detailed below. The complete mechanism is freely available at <http://c3.nuigalway.ie/mechanisms.html>. All simulations were performed using the HCT [50] chemical kinetic modeling code. For the shock-tube experiments, adiabatic conditions were assumed at constant volume. The RCM experiments are simulated in three phases: (i) the compression phase, and heat losses are accounted for by simulating the constant-volume phase after compression in two phases; (ii) a phase immediately after the end of compression where the greatest decrease in pressure (due to heat loss) was observed in each experiment; and (iii) a phase after this to infinite time with a more constant, and lesser, pressure decrease due to heat loss. In simulating the compression phase, we use the initial experimental mixture composition, temperature and pressure and the experimentally observed/measured compression ratio. The constant-volume phases (ii) and (iii) were simulated as adiabatic expansion processes, with a greater expansion in phase (ii) compared to phase (iii). A more detailed description of how

these simulations are performed is provided in a related work on methane/propane oxidation [41].

3.1. Unimolecular decomposition

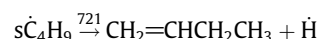
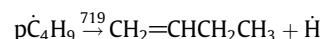
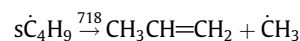
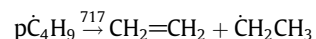
Rate constants for uni-molecular decomposition are taken from the study of Oehlschlaeger et al. [51] who reported on the high-temperature thermal decomposition of *n*-butane and isobutane behind shock waves and measured the decomposition rates of both butane isomers in the falloff regime at high temperatures using UV narrow-line laser absorption of $\dot{C}H_3$ at 216.6 nm. An RRKM/master equation analysis with a restricted (hindered) Gorin model for the transition state was carried out and fit to the experimental data, resulting in pressure-dependent rate constants which were ultimately fit using the nine-parameter Troe formalism [52].

3.2. Hydrogen abstraction

Rate constants for hydrogen abstraction were taken from the work of Orme et al. [53] who described those for abstraction of hydrogen atoms on 1° , 2° , and 3° carbons in alkanes. However, some updates have been made. For abstraction by hydroperoxyl ($\dot{H}O_2$) radical rate constants were taken from the work of Aguilera-Iparraguirre et al. [54] who used quantum chemistry at a high level of theory to calculate rates of abstractions from methane, ethane, propane and *n*- and isobutane. Carstensen et al. [55] also used quantum chemical calculations to determine rate constants for abstraction from these C_1 to C_4 alkanes by $\dot{H}O_2$, $\dot{C}H_3\dot{O}_2$, $\dot{C}_2H_5\dot{O}_2$, and other larger alkyl-peroxyl radicals. Their calculated rate constants for abstraction by $\dot{H}O_2$ radical are consistently faster than those calculated by Aguilera-Iparraguirre et al., which are at a higher level of theory, and are in better agreement with the available, albeit sparse, experimental data. Thus, we have estimated rate constants of abstraction by $\dot{C}H_3\dot{O}_2$ radical in the following way. Carstensen et al. showed that the rate constant for abstraction by $\dot{C}H_3\dot{O}_2$ radical decreased relative to $\dot{H}O_2$ radical for each type of hydrogen atom (1° , 2° , or 3°) which is consistent with its higher molecular weight. Therefore, we decreased the rate constant calculated by Aguilera-Iparraguirre et al. for $\dot{H}O_2$ radical by the same relative amount as that reported by Carstensen et al. in changing from $\dot{H}O_2$ to $\dot{C}H_3\dot{O}_2$ radical and generated three-parameter, non-Arrhenius expressions valid in the temperature range 800–1900 K for each type of hydrogen atom being abstracted. These rate constants are provided in the detailed chemical kinetic mechanism.

3.3. Alkyl radical decomposition

The first-formed radicals, *n*-butyl ($\dot{p}C_4H_9$) and *sec*-butyl ($\dot{s}C_4H_9$) can decompose primarily by β -scission, but at lower temperatures can also add to molecular oxygen to generate *n*-butyl- and *sec*-butylperoxyl radicals.



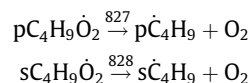
All rate constants for these reactions were taken from the work of Curran [56]. Alkyl radical β -scission reactions are endothermic processes and therefore these reactions are estimated in the reverse, exothermic direction, the addition of a smaller alkyl/alkoxy radical to an olefin with the rate constant for the decomposition of the parent radical calculated using microscopic reversibility.

3.4. Alkyl radical isomerization

n-Butyl and *sec*-butyl radicals can inter-isomerize via 1,2 and 1,3 H-shift reactions: $\dot{p}C_4H_9 \rightleftharpoons \dot{s}C_4H_9$. Rate constants of $3.56 \times 10^{10} T^{0.88} \exp(-18772/T) s^{-1}$ and $3.80 \times 10^{10} T^{0.67} \exp(-18420/T) s^{-1}$ were employed respectively for 1,2 and 1,3 H-shifts due to Matheu et al. [57], with the reverse rate calculated using microscopic reversibility.

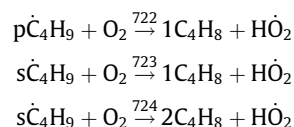
3.5. Alkyl radical addition to molecular oxygen

For the addition of the alkyl radicals to molecular oxygen:



a high-pressure limit rate constant for the addition of both *n*-butyl radical to molecular oxygen of $4.52 \times 10^{12} \text{ cm}^3 \text{ mol}^{-1} \text{ s}^{-1}$ was used, and for *sec*-butyl radical addition, a rate constant of $7.54 \times 10^{12} \text{ cm}^3 \text{ mol}^{-1} \text{ s}^{-1}$. Rate constants for reactions 827 and 828 were then calculated using microscopic reversibility.

For the reaction of the alkyl radicals with molecular oxygen producing an olefin and an hydroxyl radical:



rate constants were estimated based on those calculated by DeSain et al. [58] for the direct abstraction of a hydrogen atom from propane; for reaction 722 a rate constant of $8.37 \times 10^{-01} T^{3.59} \exp(-6019/T) \text{ cm}^3 \text{ mol}^{-1} \text{ s}^{-1}$ was used equal to that calculated for *n*-propyl + $O_2 = C_3H_6 + \dot{H}O_2$. For reaction 723 a rate constant of $5.35 \times 10^{-01} T^{3.71} \exp(-4692/T) \text{ cm}^3 \text{ mol}^{-1} \text{ s}^{-1}$ was used, which is half that calculated by DeSain et al. for iso-propyl + $O_2 = C_3H_6 + \dot{H}O_2$ since there are only three hydrogen atoms available in *sec*-butyl radical but there are six for the iso-propyl radical. Finally, for reaction 724 the same rate constant was used as per $\dot{p}C_4H_9 + O_2$ (reaction 722) since a secondary hydrogen atom is being abstracted in both cases (see Table 3).

3.6. H-atom abstraction from olefin

For both of the olefins 1-butene and 2-butene formed we have included abstraction of hydrogen atoms by O_2 , \dot{H} , $\dot{O}H$, \dot{O} , $\dot{C}H_3$,

Table 3

Rate constant expressions for $R\dot{O}_2$ isomerization to $\dot{Q}OOH$ radical on a per H-atom basis, ($\text{cm}^3 \text{ mol}^{-1} \text{ s}^{-1}$ Units).

Transition state ring size	Type	Rate expression		
		\mathcal{A}	n	E_a
5	Primary	1.0×10^{11}	0.0	34,500
	Secondary	1.0×10^{11}	0.0	31,850
	Tertiary	1.0×10^{11}	0.0	29,200
6	Primary	1.25×10^{10}	0.0	24,400
	Secondary	1.25×10^{10}	0.0	20,850
	Tertiary	1.25×10^{10}	0.0	19,100
7	Primary	1.56×10^9	0.0	22,350
	Secondary	1.56×10^9	0.0	19,050
	Tertiary	1.56×10^9	0.0	17,050
8	Primary	1.95×10^8	0.0	25,550
	Secondary	1.95×10^8	0.0	22,050
	Tertiary	1.95×10^8	0.0	20,050

$\dot{H}O_2$, $\dot{C}H_3\dot{O}_2$. In the case of 1-butene we have included rate constants for abstraction of the secondary allylic hydrogen atom on carbon number three, leading to the formation of $\dot{C}H_2 = \dot{C}HCHCH_3(1\dot{C}_4H_7-3)$ radical, and the primary hydrogen atom on carbon number four, generating the $\dot{C}H_2 = CH_2CH_2\dot{C}H_2(1\dot{C}_4H_7-4)$ radical. Rate constants for abstraction from carbon three generating secondary allylic hydrogen atoms are taken from the recommendations of Tsang [59] for the formation of allyl radical in propene, while abstraction of the primary hydrogen atoms are taken to equal primary hydrogen atoms in an alkane.

For abstraction from 2-butene only abstraction of primary allylic hydrogen atoms are considered, leading to the formation of the same resonantly stabilized radical ($1\dot{C}_4H_7-3$) as formed in 1-butene. In general, rate constants for abstraction of a primary allylic hydrogen atom were based on those for a secondary allylic hydrogen and on the relative difference in rate constant for abstraction of a primary and secondary hydrogen atom on an alkane.

3.7. Alkyl-peroxy radical isomerization

Rate constants for alkyl-peroxy radical isomerization are taken from the earlier work of Curran et al. [48] for iso-octane oxidation. However, activation energies for five membered ring isomerizations have been increased by 5 kcal/mol taking the work of DeSain et al. [58] on propane oxidation into account.

3.8. Direction elimination of olefin + $\dot{H}O_2$ from alkyl-peroxy radical

This reaction type was not considered previously by Curran et al. in their studies of *n*-heptane [47] and iso-octane [48]. Barckholtz et al. [60] using complete-basis-set (CBS) *ab initio* and density-functional-theory (DFT) techniques calculated high-pressure rate constants for the critical reactions associated with the combustion of propane in the temperature range 500–800 K, from a few Torr to 15 atm. For the reaction $n-C_3H_7\dot{O}_2 = C_3H_6 + \dot{H}O_2$ they calculated a rate constant of $1.89 \times 10^7 T^{1.51} \exp(-14915/T) s^{-1}$, and for $i-C_3H_7\dot{O}_2 = C_3H_6 + \dot{H}O_2$ a rate constant of $1.56 \times 10^9 T^{1.16} \exp(-15534/T) s^{-1}$ was reported. Naik [61] in his PhD thesis adopted these reactions for propane oxidation but reduced the activation energy of both of these reactions by 2 kcal/mol in order to improve model comparisons with experimental data. DeSain et al. [58] also reported on these reactions. They employed a time-dependent master equation for the $\dot{C}_2H_5 + O_2$, $i-\dot{C}_3H_7 + O_2$, and $n-\dot{C}_3H_7 + O_2$ reactions, using previously published *ab initio* characterizations of the stationary points of the systems, to produce temperature-dependent parameterizations that predicted the rate constants for formation of all of the products ($\dot{R} + O_2$, $\dot{R}O_2$, $\dot{Q}OOH$, $\dot{O}H$ + aldehydes, $\dot{O}H$ + O-heterocycles, $\dot{H}O_2$ + alkene). We have used the rate constants of DeSain et al. calculated at 10 atm, and thus for $p-C_4H_9\dot{O}_2 = 1C_4H_8 + \dot{H}O_2$ we employ a rate constant of $4.308 \times 10^{36} T^{-7.50} \exp(-19885/T) s^{-1}$, which is identical to that for the elimination of propene and a hydroperoxyl radical from *n*-propylperoxy radical. For $sec-C_4H_9\dot{O}_2 = 1C_4H_8 + \dot{H}O_2$ we employ a rate constant of $5.92 \times 10^{42} T^{-9.43} \exp(-20900/T) s^{-1}$, which is half that for elimination from iso-propylperoxy radical. Finally, for the reaction $sec-C_4H_9\dot{O}_2 = 2C_4H_8 + \dot{H}O_2$ we use the same rate constant as that for $sec-C_4H_9\dot{O}_2 = 1C_4H_8 + \dot{H}O_2$ as it involves the same size transition state and the same, secondary, hydrogen atom.

3.9. Cyclic ether formation

Rate constants for cyclic ether formation have been taken from the work of Wijaya et al. [62] who used CBS and DFT methods to calculate rates and thermochemistry for the cyclization of various

Table 4

Rate constant expressions for cyclic ether formation from QOOH radicals taken from Wijaya et al. [62] ($\text{cm}^3 \text{ mol}^{-1} \text{ s}^{-1}$ Units).

Cyclic ether ring size	Type	Rate expression		
		A	n	E_a
3	Primary	3.98×10^{12}	0.0	17,000
	Secondary	1.38×10^{12}	0.0	15,900
	Tertiary	3.09×10^{12}	0.0	13,400
4	Primary	4.47×10^{11}	0.0	21,900
	Secondary	2.04×10^{11}	0.0	19,500
	Tertiary	3.31×10^{11}	0.0	17,400
5	Primary	5.13×10^{10}	0.0	14,800
	Secondary	3.63×10^{10}	0.0	13,000

hydroperoxy alkyl radicals QOOH with up to six carbons. Rate constants for cyclic ether formation are provided in Table 4.

3.10. Alkoxy radical decomposition

Rate constants for alkoxy radical decomposition are taken from the work of Curran [56].

3.11. Addition of QOOH to O_2

The rate expressions for this class of reaction are identical to those for alkyl addition to O_2 . The reverse dissociation rate was then calculated from microscopic reversibility.

3.12. $\dot{\text{O}}_2\text{QOOH}$ Isomerization to Carbonylhydroperoxide + $\dot{\text{O}}\text{H}$

The rate constant for this and other isomerizations via an internal hydrogen atom transfer are analogous to those for $\text{RO}_2 = \text{QOOH}$ isomerization. Similar to the Curran et al. *n*-heptane and iso-octane work, the activation energy has been reduced by 3 kcal/mol as the hydrogen atom being abstracted is bound to a carbon atom which is bound to a hydroperoxyl group and should be more easily removed. Rate constant for this class of reaction are provided in Table 5.

4. Results and discussion

All ignition delay times measured in both the shock tube (ST) and in the RCM are provided in Tables 1–21 of Supplemental material. Fig. 3a shows a comparison between experiment (line and

Table 5

Rate constant expressions for $\dot{\text{O}}_2\text{QOOH}$ isomerization to carbonyl-hydroperoxide ($n\text{C}_4\text{ketxy}$) + $\dot{\text{O}}\text{H}$ on a per H-atom basis ($\text{cm}^3 \text{ mol}^{-1} \text{ s}^{-1}$ Units).

Transition state ring size	Type	Rate expression		
		A	n	E_a
5	Primary	1.0×10^{11}	0.0	31,500
	Secondary	1.0×10^{11}	0.0	28,850
	Tertiary	1.00×10^{11}	0.0	26,200
6	Primary	1.25×10^{10}	0.0	21,400
	Secondary	1.25×10^{10}	0.0	17,850
	Tertiary	1.25×10^{10}	0.0	16,100
7	Primary	1.56×10^9	0.0	19,350
	Secondary	1.56×10^9	0.0	16,050
	Tertiary	1.56×10^9	0.0	14,050
8	Primary	1.95×10^8	0.0	22,550
	Secondary	1.95×10^8	0.0	19,050
	Tertiary	1.95×10^8	0.0	17,050

point) and simulation (line) pressure versus time traces for $\phi = 1.0$, 20 atm. Simulations were performed as described above in the description of the model and in our previous work on methane/propane [41] mixtures. The first experimentally recorded cool flame event at these conditions was recorded 734 K. Here, the cool flame is exhibited after 11.8 ms (2.6 ms before total ignition) as a 1.2 atm pressure rise. As the temperature of the experiment is increased to 761 K, cool flame behavior occurs sooner, at 5.3 ms. The magnitude of the resulting pressure rise is reduced to 1.1 atm and the delay between the occurrence of this pressure rise and the onset of total ignition lengthens to 3.46 ms. This trend continues into the NTC region, as at 804 K the pressure rise due to cool flame chemistry becomes 0.5 atm and the time lag to the total ignition event increases to 6.1 ms. When a temperature of 850 K is reached, cool flame chemistry is almost indistinguishable. It appears after 4.7 ms as a pressure rise of 0.2 atm, 6.2 ms later total ignition occurs. No other cool flame events were recorded experimentally above this temperature.

These findings are similar to those of the Westbrook et al. [63] investigations into the cool flame chemistry of *n*-pentane, where it was observed that, at higher temperatures, the pressure rise accompanying cool flame chemistry was reduced. The model accurately predicts the onset of the cool flame at the three lowest temperatures and although it does not accurately capture the magnitude of the cool flame pressure rises it does show trends identical to those found experimentally. The model predicts the highest cool flame pressure rises at the lowest temperatures, and it also predicts the lengthening of the lag time between the onset of cool-flame reactivity and total ignition as temperature increases. The model does not however reproduce the cool flame chemistry at 850 K, but the scale of the cool flame event is far less than those of the lower-temperature experiments.

Fig. 3b depicts model-predicted temperature versus time profiles for *n*-C₄H₁₀ oxidation in “air”, $\phi = 1.0$, $p_c = 20$ atm. The model predicts that, at temperatures above approximately 920 K, there is a rapid rise in temperature leading to the second-stage ignition event. A discussion of the mechanism responsible for this was published previously [63], but is re-enforced here. Within the system, hydroperoxyl radicals are produced, primarily by the reaction of molecular oxygen with a stable molecule but also via the concerted elimination channel, $\text{RO}_2 = \text{olefin} + \text{HO}_2$. The HO_2 radicals then react primarily via two reactions: $\text{HO}_2 + \text{HO}_2 = \text{H}_2\text{O}_2 + \text{O}_2$ and $\text{RH} + \text{HO}_2 = \text{R} + \text{H}_2\text{O}_2$. The activation energy for H_2O_2 decomposition is large enough (≈ 45 kcal/mol) that its decomposition is still quite slow in the low-temperature range (600–900 K). At temperatures above this, the rate of hydrogen peroxide decomposition accelerates until it begins to provide significant chain branching, producing two $\dot{\text{O}}\text{H}$ radicals for each H_2O_2 species consumed. At the pressures of this study, as well as in internal combustion engines close to knocking operation, rapid decomposition of H_2O_2 leading to hot ignition is observed at temperatures slightly above 900 K.

Figs. 4 and 5 present the results of the experiments in comparison to the predictions of the detailed mechanism. As anticipated, increasing pressures also led to decreasing ignition times, Fig. 4. For all mixtures and for the relatively low- to intermediate-temperature conditions of this study, rich mixtures are fastest to ignite, then stoichiometric, with lean mixtures slowest, Fig. 5, which follows the generally accepted understanding of fuel oxidation kinetics under these conditions.

4.1. Effect of pressure on ignition

Fig. 4a–d shows comparisons of experimental results versus model predictions for various butane mixtures at equivalence ratios of 0.3, 0.5, 1.0 and 2.0. Fig. 4a shows results for a 0.96%

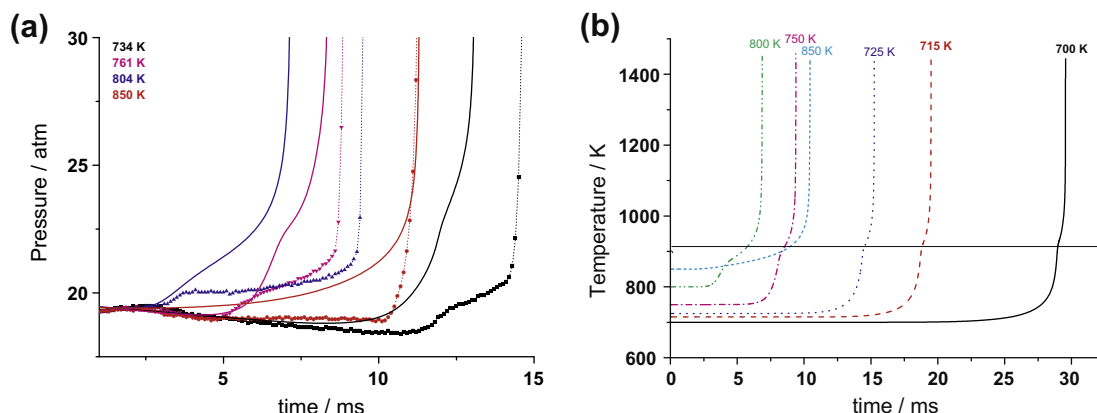


Fig. 3. Experimental (RCM) and model-predicted pressure versus time profiles (a) and model-predicted temperature versus time profiles (b) for $n\text{-C}_4\text{H}_{10}$ oxidation in “air”, $\phi = 1.0$, $p_c = 20$ atm.

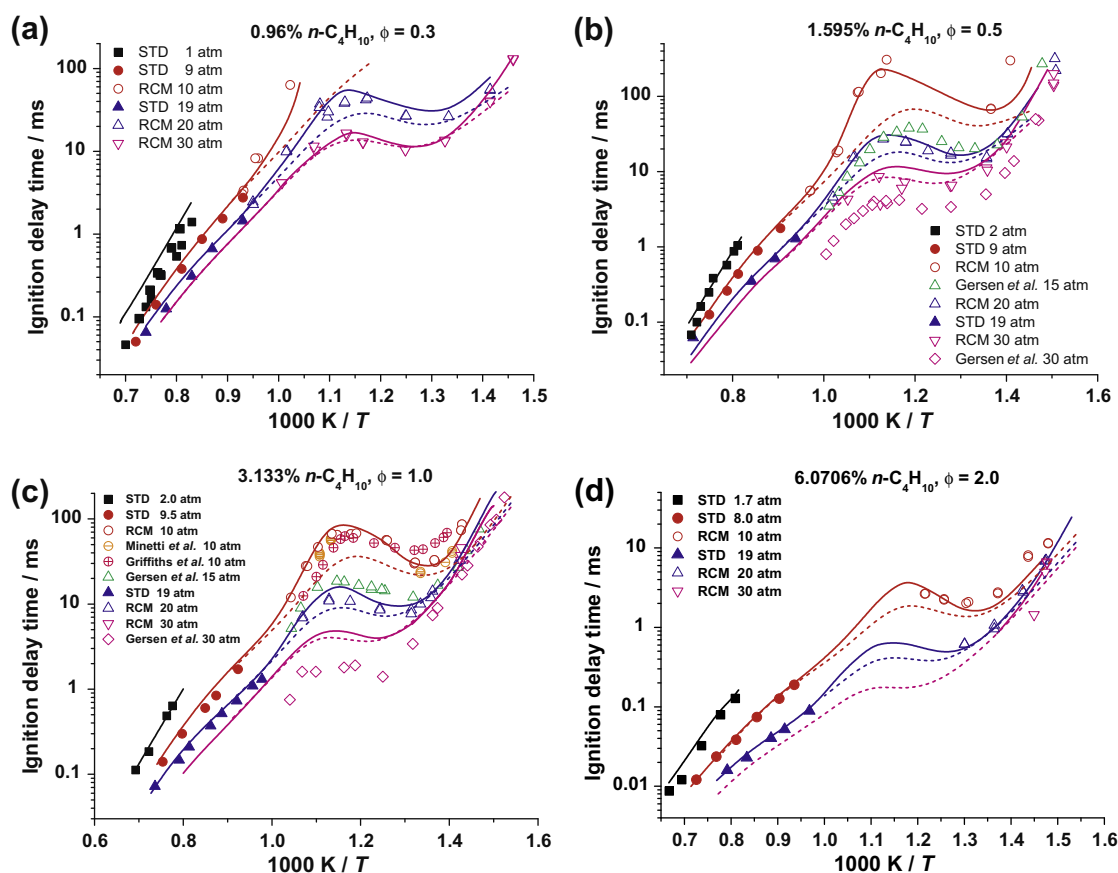


Fig. 4. Effect of pressure on ignition delay times for $n\text{-C}_4\text{H}_{10}$ oxidation in “air”, lines are model simulations, solid lines include heat losses, dashed lines assume adiabatic conditions. STD = shock-tube data.

$n\text{-C}_4\text{H}_{10}$ mixture at $\phi = 0.3$ in “air” at pressures of approximately 1, 10, 20, and 30 atm. It is apparent that reactivity increases with increasing pressure, as a decrease in ignition delay time is observed with an increase in pressure at constant temperature. Furthermore, the effect of increasing pressure is most pronounced in the NTC region over the temperature range 740–1000 K.

This figure (Fig. 4) shows the complementary nature of the RCM/shock-tube study; the shock-tube data are recorded in the temperature range 1000–1430 K, while the RCM data extend the temperature range of study from 1000 K to 670 K, approximately. Moreover, a direct comparison of shock-tube and RCM experimental results is available at several pressures, namely 10, 20, and

30 atm, and although there are few data points at a common temperature, it is clear that both the RCM and shock-tube data sets are consistent. At 10 atm, the fuel does not react below 1000 K, while at 20 and 30 atm the fuel reacts at temperatures of 700 and 670 K, respectively, and exhibits NTC behavior in the temperature range 670–1000 K. The mechanism is in very good agreement with the experimental results for the higher-pressure conditions, but is approximately 20–30% slower than experiment at 1 atm.

Fig. 4b shows the effect of pressure for a 1.614% n -butane mixture at $\phi = 0.5$ in “air” at pressures of approximately 2, 10, 15, 20 and 30 atm. Included are data that were recorded by Gersen et al. [64]. Again, the RCM data show that reactivity starts at 660 K in the

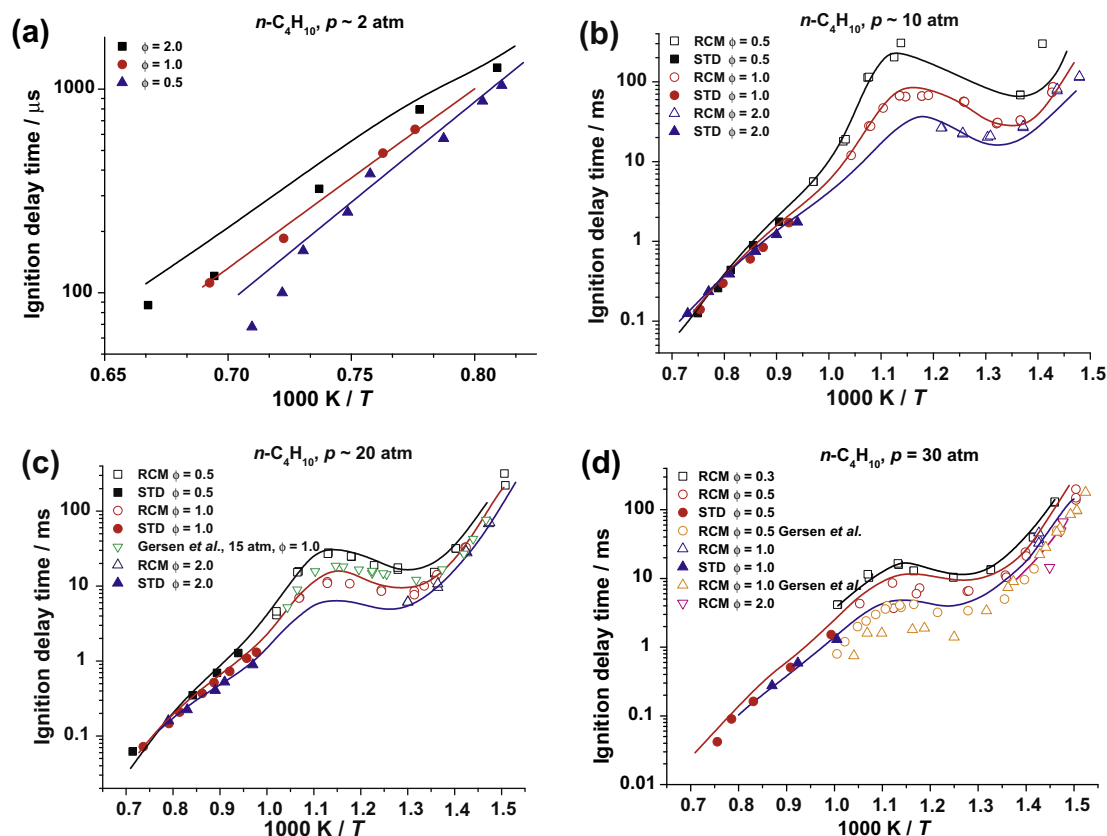


Fig. 5. Effect of equivalence ratio on ignition delay times for $n\text{-C}_4\text{H}_{10}$ oxidation in “air”, lines are model simulations.

case of the 20 and 30 atm data but starts at 715 K at the lower pressure of 10 atm. Comparing the current experimental RCM data with that reported by Gersen et al., the present data at 20 atm show slightly faster reactivity to that of Gersen et al. in the temperature range 650–900 K, but are slightly slower at temperatures above 900 K. Furthermore, a direct comparison of the present RCM data to those of Gersen et al. exists at 30 atm, where their data are approximately twice as fast as the data herein. Shock-tube data were taken at an average pressure near 45 atm and are displayed in Fig. 4b at an adjusted pressure of 30 atm. This adjustment was performed using the pressure dependence derived from the shock-tube data, described in more detail below in the section containing the ignition delay time correlations. At 30 atm, the model well reproduces both the RCM and the ST data taken in the present study but is slightly slow in the NTC region.

Similar comparisons depicting the effect of pressure are shown for a 3.133% n -butane mixture at $\phi = 1.0$ in “air” at 2, 10, 15, 20, and 30 atm pressure, Fig. 4c. In this graph we have also included the data of Minetti et al. [6–8] and Griffiths et al. [10] at 10 atm and Gersen et al. at 15 and 30 atm. As mentioned in the previous paragraph, the 45-atm shock-tube data are plotted in Fig. 4c at an adjusted pressure of 30 atm to better compare with the available RCM and literature data at that pressure without cluttering the plot. The present data at 10 atm agree well with the data of Minetti et al. throughout the accessible range of temperature, while those of Griffiths et al. are slower below 770 K and faster above 900 K, but do agree well with the other RCM data at temperatures intermediate to this. The model too is in good agreement with the experimental results at 2, 10 and 20 atm. The model also agrees with the measured ST data at 30 atm but is considerably (more than three times) slower compared to the 30-atm experimental RCM results of Gersen et al. It should be noted that compar-

isons between different RCM measurements must be performed with caution, because of non-ideal behavior, usually due to different delays for the “same” conditions, but even in the same facility different inert gas compositions can give substantially different delay times [65,66]. We have not been provided with pressure versus time profiles for “un-reactive” mixtures for any of the other RCM experimental data presented in these figures, and thus cannot simulate the corresponding heat losses as we have done for our own data.

Finally, in Fig. 4d the effect of pressure for a 6.07% n -butane mixture at $\phi = 2.0$ in “air” is shown. Again it is apparent that increasing the pressure reduces ignition delay times and increases the reactivity of the system. The model is in excellent agreement with the experimental results at 1.7, 8–10 and 20 atm. However, at 30 atm the model is slower than the experiment at 690 K, but the limited experimental temperature range available leaves the overall model performance inconclusive at this pressure.

While it is true that the RCM data encompass the low-temperature regime in which ignition times are long and heat losses are significant, however at the higher temperature end of the RCM study ignition times become short, ≤ 10 ms, and heat losses become relatively small. Thus, it should be expected that the RCM and shock tube data should agree at the point of overlap of both sets of data. Moreover, the reader should be aware that the temperature (or inverse temperature in this case) reported on the x-axis is the compressed-gas temperature corresponding to the measured compressed-gas pressure when the pistons stop. Thereafter, there is a significant pressure drop after compression resulting in significant heat losses but this is included in our simulation as explained earlier. To depict the effect on our simulations of including heat losses we have also simulated all profiles in Fig. 4 under adi-

adiabatic conditions, depicted as dashed lines. One can clearly see that at long ignition times heat losses significantly inhibit ignition times while at higher temperatures, where ignition times are shorter, both the heat loss and adiabatic simulations predict almost identical ignition times. For the lean, low-pressure experiments where gas densities are lowest, heat losses are greatest, Fig. 4a and b, while for fuel-rich mixtures at high pressure (30 atm) heat losses are lowest and including/excluding heat loss in the simulation does not have a significant effect on predictions, Fig. 4d.

4.2. Effect of equivalence ratio on ignition

Fig. 5a–d illustrates the effect of equivalence ratio on ignition delay times. Fig. 5a shows data recorded for *n*-butane mixtures at equivalence ratios of 2, 1.0, and 0.5 in “air” at a pressure of approximately 2 atm (the lean data were recorded at an average pressure of 1.7 atm). At these low-pressure and relatively high-temperature conditions, fuel-lean mixtures are most reactive while fuel-rich mixtures are slowest to ignite at any given temperature. This is common to all alkane fuels under these conditions where the rate of the dominant chain-branching reaction $\text{H} + \text{O}_2 \rightarrow \dot{\text{O}} + \text{OH}$ depends on the concentration of molecular oxygen. In Fig. 5b–d, the dependence on equivalence ratio is reversed; at these lower-temperature, higher-pressure conditions, fuel-lean mixtures are slowest to ignite, with the fuel-rich mixtures fastest, due to the main chain-branching reactions emanating from the fuel. This effect is more pronounced at temperatures below about 1000 K, as discussed in more detail below.

Fig. 5a also shows that there is excellent agreement between the model and experiment at $\phi = 0.5$ and 1.0, but for fuel-rich mixtures ($\phi \geq 2.0$) the model tends to slightly ($\approx 30\%$) over-predict ignition delay times. Fig. 5b shows data recorded for *n*-butane mixtures in air at 10 atm pressure. At low temperatures (650–1000 K), lean mixtures are slowest to ignite, whereas rich mixtures are fastest. The greatest dependence on equivalence ratio occurs in the NTC region, in the temperature range 740–910 K. However, when the temperature reaches approximately 1250 K, all mixtures be they rich, stoichiometric, or lean all ignite at approximately the same time. This is the point at which the chemical kinetic behavior transitions from low/intermediate reactivity, where the fuel radical species dominate and control the overall reactivity, to high-temperature kinetics where the $\text{H} + \text{O}_2$ chain-branching reaction dominates. There is overall excellent agreement between the mechanism and the data for these mixtures.

Fig. 5c shows data recorded for *n*-butane mixtures at 20 atm pressure. Again, the same trends as observed at 10 atm are seen, in that at low temperatures (650–1000 K) the lean mixtures are slowest to ignite and rich mixtures are fastest. At 20 atm, there appears to be a lesser dependence of ignition delay time on equivalence ratio compared to that observed at 10 atm. This is probably attributable to greater heat losses at 10 atm compared to 20 atm. In this figure too are plotted the data recorded by Gersen et al. [64] at $\phi = 1.0$ albeit at an average compressed-gas pressure of 15 atm. Their data and those recorded in this study are in relatively good agreement. Moreover, there is overall excellent agreement between the mechanism and the data for these mixtures.

Finally, Fig. 5d shows data recorded for *n*-butane mixtures at 30-atm pressure. The reported shock-tube data are the same as those depicted in Fig. 4b and c, and have been adjusted to 30 atm. Again, the same trends are observed here as were seen at 10 and 20 atm, in that lean mixtures are slowest to ignite at low temperatures and rich mixtures are fastest. In this figure, the data recorded by Gersen et al. [64] at $\phi = 0.5$ and 1.0 are also plotted. At an equivalence ratio of 0.5, it is evident again that the present data (both ST and RCM) are consistently approximately a factor of two slower than those recorded by Gersen et al. The model too predicts

slightly slower reactivity than we observed at $\phi = 0.5$ but is substantially slower than the data recorded by Gersen et al. for lean and stoichiometric conditions.

In both Figs. 4 and 5 where experimental overlap exists, usually at approximately 1000 K, between the RCM data (taken at NUI Galway) and the shock-tube data (recorded at Texas A&M University), both sets of data are in excellent agreement. We observed this agreement also in our previous work for methane/propane [41] and methane/ethane/propane [67] mixtures.

4.3. Ignition delay time correlations

Using the shock-tube results from all four mixtures, correlations have been developed to predict ignition delay times as a function of temperature, pressure and concentration of fuel and air. The basic form of the correlation is as follows:

$$\tau_{\text{ign}} = A[\text{FUEL}]^x[\text{AIR}]^y \exp(E/RT)$$

where τ_{ign} is the ignition delay time or kinetic time in μs ; FUEL is the fuel concentration in mol/cm^3 ; AIR is the air concentration in mol/cm^3 ; and E , A , x , and y are constants. The constant E is commonly referred to as an ignition activation energy which is in kcal/mol , and R is the ideal gas constant in $\text{kcal}/\text{mol K}$ units. From the above equation, it can be seen that the ignition delay time is exponentially dependent on the inverse temperature and directly dependent on the mixture concentration to some power. Additionally, the pressure dependence of ignition delay can be estimated as pressure raised to the sum of the exponents of the fuel and air terms since the Fuel and Air concentrations both depend linearly on the pressure.

When examining the experimental ignition time results, a shift in temperature dependence is observed between the higher- and intermediate-temperature data at around 1175 K. Due to this slight shift, two separate correlations were developed to describe both the high- and intermediate-temperature data. When developing the high- and intermediate-temperature correlations, temperatures that were around 1175 K were used to in both so that the correlations would overlap. The correlation does not apply to temperatures below 1025 K where NTC behavior is seen. The low-temperature region cannot be described by the typical Arrhenius-type equation. Developing a low-temperature correlation is cumbersome and not the focus of this study.

The resulting high-temperature correlation ($1175 < T < 1430 \text{ K}$) is

$$\tau_{\text{ign}} = 1.862 \times 10^{-7} [n - \text{C}_4\text{H}_{10}]^{0.16} [\text{AIR}]^{-0.73} \exp(40.3/RT)$$

The corresponding intermediate-temperature correlation ($1025 < T < 1175 \text{ K}$) is

$$\tau_{\text{ign}} = 7.892 \times 10^{-7} [n - \text{C}_4\text{H}_{10}]^{-0.34} [\text{AIR}]^{-0.70} \exp(28.0/RT)$$

Burcat et al. [12] performed shock-tube experiments of *n*-butane in argon-simulated-air mixtures over the range of high temperatures similar to that examined in this study and found the ignition activation energy to be roughly 40 kcal/mol , which agrees well with the activation energy shown above for the high-temperature correlation. Fig. 6 shows good agreement between the correlations, experimental results, and the mechanism predictions.

5. Reaction path and sensitivity analysis

A reaction path analysis was carried out for the RCM conditions outlined in Fig. 7, at 20 atm pressure, at an equivalence ratio of 1.0, at 830 K, which is an “average” experimental condition and lies in the middle of the NTC region. The reaction scheme shows that the fuel undergoes hydrogen atom abstraction mainly by $\dot{\text{O}}\text{H}$ radical,

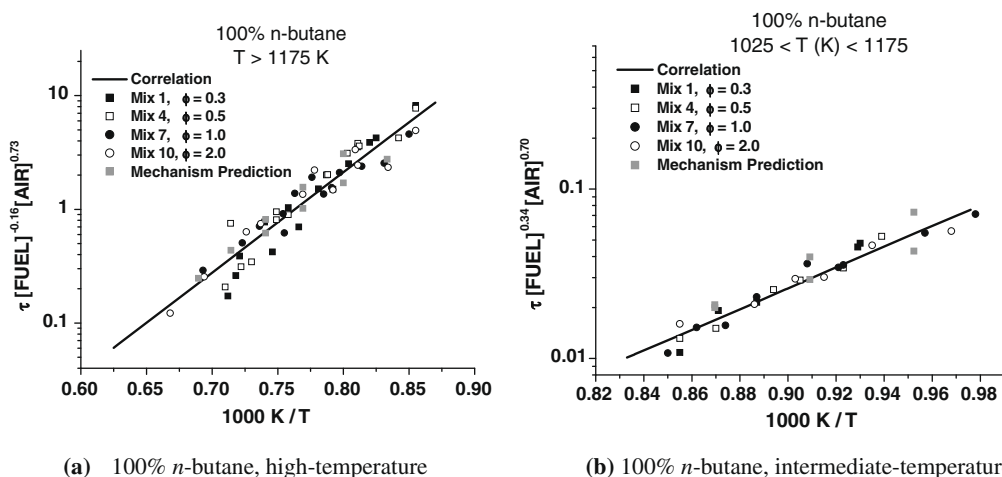
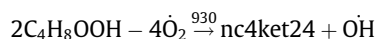
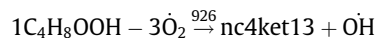


Fig. 6. Experimental data, correlation results, and mechanism predictions plotted against inverse temperature show good agreement at both high (left) and intermediate (right) temperatures. A shallower slope, corresponding to a lower ignition activation energy, is seen at intermediate temperatures (28.0 versus 40.3 kcal/mol). τ_{ign} in μs , $[\text{FUEL}]$ and $[\text{AIR}]$ in mol/cm^3 .

with a smaller contribution from HO_2 radical and H atom, producing n -butyl radical, which accounts for 32.4% of total fuel consumed, and sec -butyl radical, which accounts for 67.6% of the fuel. The n -butyl radical formed undergoes β -scission to form ethylene and an ethyl radical and/or adds to molecular oxygen to generate n -butylperoxy radical at almost equal rates. The sec -butyl radical can also add to molecular oxygen (80%) or undergo β -scission (20%) to form propene and a methyl radical. For both the n -butylperoxy radical and the sec -butylperoxy radical, the main consumption route is via the molecular elimination channel to form 1- or 2-butene and a hydroperoxyl radical. These olefins (66%) add with hydroxyl radical to form an alkyl-hydroxide radical which then adds to molecular oxygen, undergoes an internal hydrogen atom isomerization and decomposes in what is conventionally considered the Waddington mechanism [68,69]. Alternatively, the butene isomers can undergo hydrogen atom abstraction (33%), yielding mainly the resonantly stabilized but-1-en-2-yl radical. Only a relatively small fraction ($\leq 20\%$) of the butylperoxy radicals undergo internal hydrogen-atom isomerization to yield hydroperoxy-butyl radicals.

Under these conditions, a minor route consuming both n - and sec -butylperoxy radicals involves an internal hydrogen atom isom-

erization via a six-centered transition-state ring producing the hydroperoxy alkyl radicals $1\dot{\text{C}}_4\text{H}_8\text{OOH} - 3$ and $2\dot{\text{C}}_4\text{H}_8\text{OOH} - 4$, respectively. These radicals are important to chain-branching as, at low temperatures, they add to molecular oxygen and undergo a second internal hydrogen isomerization, ultimately leading to chain branching.



It has been observed in the past [47,48] that isomerizations proceeding through five-membered rings produce hydroperoxy-alkyl radicals that lead to the formation of an olefin and a hydroperoxyl radical, while isomerizations involving seven-membered transition-state rings produce hydroperoxy-alkyl radicals that generate high concentrations of cyclic ethers and an hydroxyl radicals.

Secondary hydrogen atoms are easier to abstract compared to primary ones (with bond dissociation energies of 98.5 and 101.5 kcal/mol respectively) and thus secondary alkyl radicals are formed in greater abundance compared to primary ones, with sec -butyl radical accounting for 67% of the fuel flux shown in Fig. 7, while 33% of the fuel forms n -butyl radical. In the same

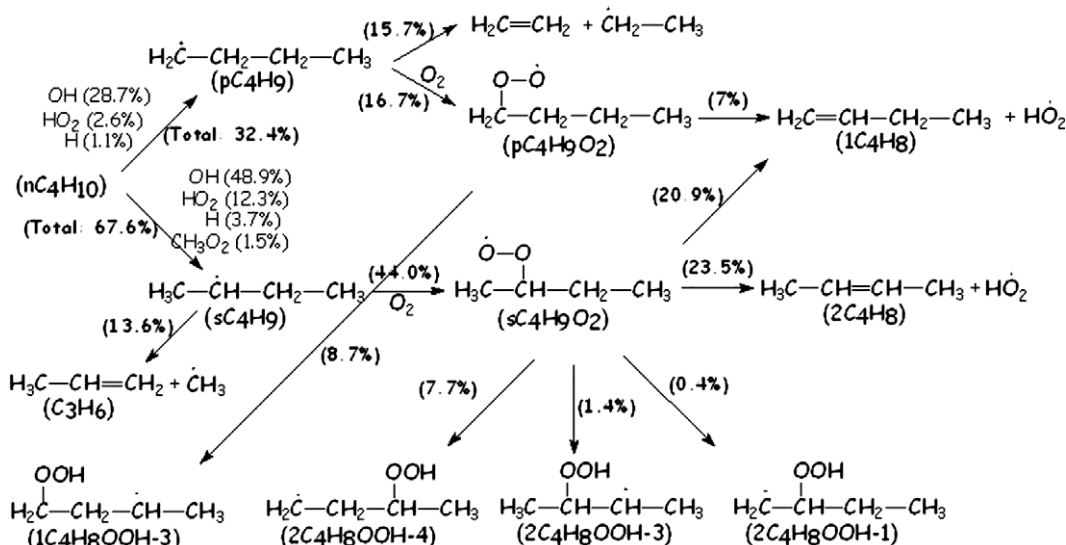


Fig. 7. Reaction path analysis for n -butane in a RCM; $\phi = 1$, 830 K, 20 atm, 20% consumption.

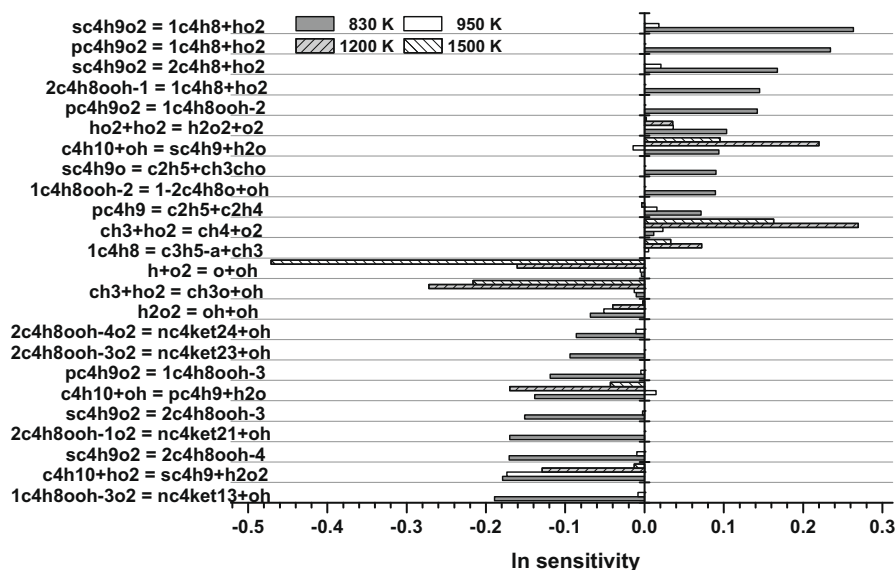


Fig. 8. Sensitivity coefficients showing the effect of temperature on *n*-butane ignition time, $\phi = 1.0$, $p = 20$ bar.

way internal hydrogen atom isomerizations involving secondary hydrogen atoms are favoured over primary ones, but only in the case of *n*-butylperoxy radical isomerization to $1C_4H_8OOH-3$ do we have a six-membered transition state involving a secondary hydrogen atom. The isomerization of *sec*-butylperoxy radical to $2C_4H_8OOH-4$ involves a primary hydrogen atom with a higher activation energy barrier and lower rate constant. Thus, in the *n*-butane system, the main low-temperature chain-branching route through six-membered transition-state rings for isomerization of alkyl-peroxy radicals to hydroperoxy-alkyl radicals and the second isomerization of the peroxy-hydroperoxy-alkyl radical to form a ketohydroperoxide and an hydroxyl radical are limited. This can explain (and confirm) the observations of Griffiths et al. [10] that *n*-butane is relatively un-reactive compared to other larger *n*-alkanes and that this was associated with the failure to form di-peroxy species readily.

A sensitivity analysis was performed to investigate reaction sensitivity to ignition time for *n*-butane oxidation as a function

of temperature, Fig. 8 and equivalence ratio, Fig. 9. The analyses were performed by increasing and decreasing both the forward and reverse rate constants by a factor of two, with sensitivities expressed using the formula:

$$\ln S = \frac{\ln(\tau_+/\tau_-) / \ln(k_+/k_-)}{\ln(k_+/k_-)} = \frac{\ln(\tau_+/\tau_-)}{\ln(2/0.5)}$$

Fig. 8 depicts sensitivity coefficients for a stoichiometric *n*-butane/air mixture at 830, 950, 1200, and 1500 K and at a pressure of 20 atm. Sensitivity coefficients under lean and rich conditions are also provided in Figs. 1 and 2 of Supplemental material, but for all equivalence ratios, the sensitivities are essentially the same. A positive sensitivity indicates an increase in the ignition time and thus a decrease in overall reactivity, conversely a negative value indicates a decrease in ignition delay time and thus an increase in overall reactivity. Note that the only primary fuel reactions showing sensitivity at higher temperature (1200 and 1500 K) are hydrogen atom abstraction from the fuel by $\dot{O}H$ and $H\dot{O}_2$ radicals.

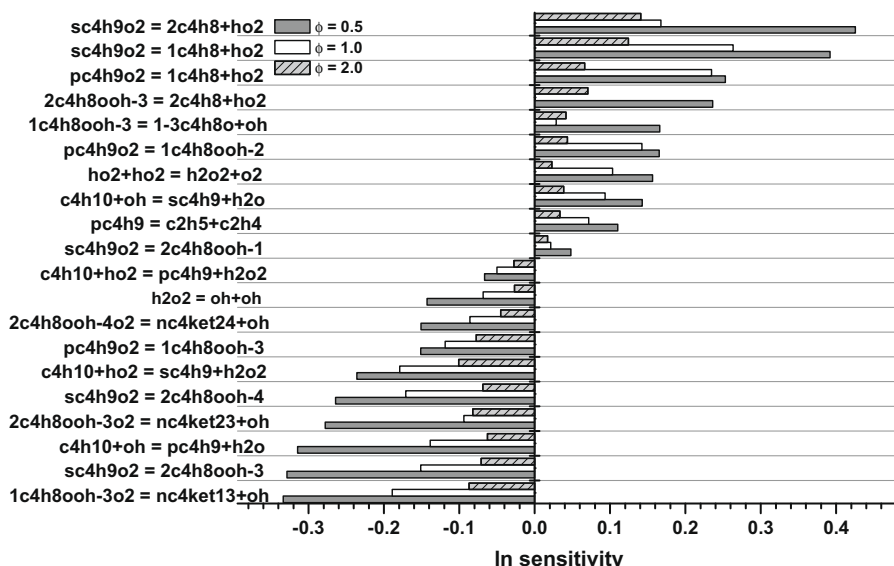
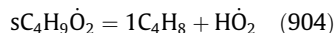
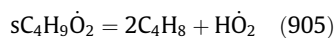


Fig. 9. Sensitivity coefficients showing the effect of equivalence ratio on *n*-butane ignition time, $T = 830$ K, $p = 20$ bar.

Other important reactions include the main chain-branching reaction at higher temperatures ($H + O_2 = \dot{O} + \dot{OH}$), and methyl radical reaction with hydroperoxyl radical, with the chain branching reaction $\dot{C}H_3 + \dot{H}O_2 = CH_3\dot{O} + \dot{OH}$ promoting reactivity, while the chain termination reaction $\dot{C}H_3 + \dot{H}O_2 = CH_4 + O_2$ inhibiting reactivity.

The reactions with the highest positive sensitivity coefficients (most inhibiting) at 830 K at all three equivalence ratios are the concerted elimination of 1- and 2-butene and a hydroperoxyl radical from *n*- and *sec*-butylperoxy radicals. These are propagation reactions and thus lead to reduced reactivity and are known to contribute to the NTC behavior of the fuel [58].



By contrast, the reaction with the largest negative sensitivity at 830 K is the isomerization of a peroxy-butylhydroperoxide to produce the corresponding stable carbonyl-hydroperoxide species and an hydroxyl radical ($1C_4H_8OOH - 3O_2 = nC_4ket13 + \dot{OH}$). This reaction is important because the carbonyl-hydroperoxide will further decompose to yield a carbonyl-alkoxy radical and a second hydroxyl radical, and thus this sequence is the main chain-branching process at low temperatures.



Reactions in which butylperoxy radical produce a conjugate olefin and a $\dot{H}O_2$ radical inhibit the reactivity of the system, as these reactions compete with possible chain-branching reactions in which the butylperoxy radicals undergo isomerization to hydroperoxy-butyl radical, which can then add to molecular oxygen and proceed through the chain-branching mechanism described above.

It is interesting to note that increasing the rate of hydrogen abstraction from the fuel to generate *sec*-butyl radicals inhibits reactivity, whereas abstraction forming *n*-butyl radicals and water promotes reactivity. As we observe in the rate of production analysis, Fig. 7, slightly more hydroperoxy-butyl radical ($1\dot{C}_4H_8OOH - 3$) is produced from *n*-butylperoxy radical than ($2\dot{C}_4H_8OOH - 4$) from *sec*-butylperoxy radical. It is these radicals that mainly add to molecular oxygen and proceed through the low-temperature chain-branching mechanism and so increasing the production of the ($1\dot{C}_4H_8OOH - 3$) radical ultimately leads to an increased overall reactivity at lower temperatures. Similarly, increasing the rate of isomerization of *n*-butyl radical to *sec*-butyl radical also inhibits reactivity at 830 K.

Finally, the decomposition of *n*-butyl radical to ethylene and ethyl radical inhibits reactivity at 830 K, and shows a decreasing sensitivity at higher temperatures. This is because at lower temperatures this reaction competes with addition to molecular oxygen and at 830 K, increasing the rate of alkyl radical decomposition reduces the rate of alkyl-peroxy radical formation and subsequent chain-branching reactions.

Fig. 9 depicts sensitivity coefficients as a function of equivalence ratio for *n*-butane/air mixtures at 830 K and at a pressure of 20 atm. Here we see higher sensitivity coefficients for lean conditions compared to stoichiometric, while rich conditions show lowest sensitivity. However, we note the same important reactions as observed in Fig. 8, in that concerted elimination reactions from butylperoxy radicals are the most important inhibiting reactions, while the reactions leading to the formation of the carbonyl-hydroperoxide species and an hydroxyl radical (the main chain-branching reactions) are among those most promoting reactivity. Reactions in which a six-membered transition-state ring is formed all promote reactivity (e.g. $pC_4H_9\dot{O}_2 = 1\dot{C}_4H_8OOH - 3$, $1C_4H_8OOH - 3\dot{O}_2 = nC_4ket13 + \dot{OH}$, $sC_4H_9\dot{O}_2 = 2\dot{C}_4H_8OOH - 4$, in addition to $2C_4H_8OOH - 4\dot{O}_2 = nC_4ket24 + \dot{OH}$).

A sensitivity analysis to equivalence ratio was also performed at 950 and 1200 K, Figs. 3 and 4 of Supplemental material. At 950 K we see higher sensitivity coefficients for rich mixtures compared to stoichiometric, while lean conditions show lowest sensitivity coefficients, which is the opposite trend to that observed at 830 K. This is due to the fact that at 950 K $\dot{H}O_2$ radical chemistry is more important than at 830 K. At 950 K and at $\phi = 2.0$, the most promoting reaction is: $C_4H_{10} + \dot{H}O_2 = s\dot{C}_4H_9 + H_2O_2$, which indicates the importance of the hydroperoxyl radical at this temperature (and pressure). The reaction which is most inhibiting ($\dot{H}O_2 + \dot{H}O_2 = H_2O_2 + O_2$) involves the self-reaction of hydroperoxyl radical to generate hydrogen peroxide and molecular oxygen. This reaction consumes two hydroperoxyl radicals, producing only one hydrogen peroxide molecule which subsequently decomposes into two hydroxyl radicals (chain branching). This reaction thus competes with other $RH + \dot{H}O_2 = \dot{R} + H_2O_2$ reactions in which only one $\dot{H}O_2$ radical generates one hydrogen peroxide molecule. At this temperature we see that most of the classical low-temperature chemistry no longer shows significant sensitivity. Moreover, unimolecular fuel decomposition reactions start to show positive sensitivities and also alkyl radical decomposition reactions also show some sensitivity, both positive and negative. At 1200 K, Fig. 4 of Supplemental material, we see that the dominance of the hydroperoxyl radical has been replaced by $\dot{C}H_3 + \dot{H}O_2$ and $H + O_2 = \dot{O} + \dot{OH}$ chemistry in addition to the increasing importance of uni-molecular fuel decomposition reactions and hydrogen atom abstraction reactions from the fuel by hydrogen atom and methyl radical in addition to hydroxyl and hydroperoxyl radicals which dominate hydrogen atom abstraction from the fuel at lower temperatures.

6. Comparison with other shock-tube measurements

Burcat et al. [12], studied the oxidation of *n*-butane for stoichiometric argon-simulated-air mixtures in a reflected-shock study of the alkanes from methane through pentane. With the exception of ethane, the ignition delay times decreased with increasing number of carbon atoms, though differences amongst the various fuels were not large. Fig. 10 shows a comparison of the current model together with the experimental data of Burcat et al. and also additional data taken for the present study to further validate this set of conditions. The new data for this mixture are provide in Table 21 of Supplemental material. There is overall excellent agreement amongst both data sets and the model predictions.

Horning et al. [13] measured ignition times for propane, *n*-butane, *n*-heptane, and *n*-decane behind reflected shock waves over the temperature range 1300–1700 K, and in the pressure range

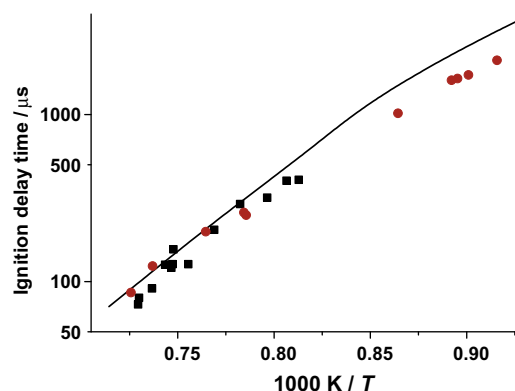


Fig. 10. Experimental ■ – Burcat et al. [12], ● – present work *n*-butane ignition times for 2.5% *n*-butane, 16.25% O_2 , 81.25% Ar, $p_5 \approx 10$ atm

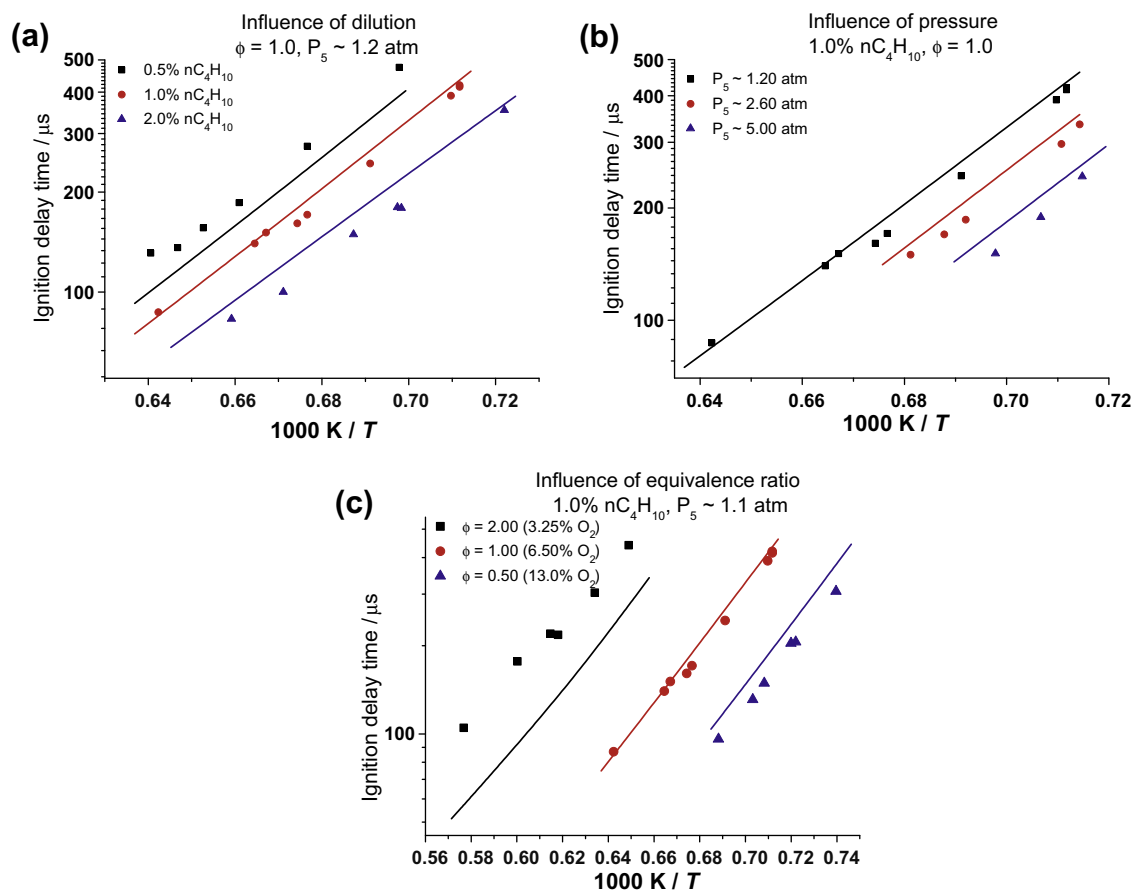


Fig. 11. Comparison of ignition delay times for dilute n -C₄H₁₀ oxidation in Ar, points are experimental results from Horning et al. [13], lines are model simulations.

1–6 atm. For n -butane, the test mixture composition varied from 3.25–13.0% O₂, at equivalence ratios of 0.5, 1.0 and 2.0. Fig. 11 shows a comparison of the current model together with the experimental data of Horning et al. There is overall very good agreement between the experimental and the model predictions, but there is a trend in that rich mixtures are predicted to be faster than experiment while ignition delay predictions for lean mixtures are slower than experiment.

Fig. 11a shows the effect of dilution under stoichiometric conditions and at an average reflected-shock pressure of 1.2 atm. As seen in the plot, the more concentrated the mixture the faster is the ignition time. Fig. 11b depicts the influence of pressure for 1.0% n -butane/6.5% oxygen/92.5% argon, at average reflected-shock pressures of 1.2, 2.6, and 5.0 atm. Again it can be observed that as the pressure increases, which is an effective increase in concentration, the ignition time becomes faster. Finally, Fig. 11c shows the influence of equivalence ratio for 1.0% n -butane/oxygen mixtures diluted in argon at an average reflected-shock pressure of 1.1 atm. Here is observed the large effect of oxygen concentration on ignition delay times in which each doubling of oxygen concentration leads to a substantial decrease in ignition delay times.

7. Conclusions

Autoignition delay time measurements were recorded at equivalence ratios of 0.3, 0.5, 1, and 2 for n -butane at pressures of approximately 1, 10, 20 and 30 atm at temperatures from 690 to 1430 K in both a rapid compression machine and in a shock tube, resulting in the most comprehensive set of ignition data for n -butane available thus far in the literature. It was found that these data

agree quite well with others available in the literature recorded by Minetti et al. [6–8] and Griffiths et al. [10] at 10 atm but was generally slower than those recorded by Gersen et al. [64] at 15 and 30 atm. Good agreement for the present results was also seen when compared to the studies of Burcat et al. [12] and Horning et al. [13].

A detailed chemical kinetic model consisting of 1328 reactions involving 230 species was constructed and used to predict the ignition delay times. Overall, there is very good agreement between the model and experiment given the extensive range of experimental conditions studied in both the present work and those available in the literature. It was found that one of the most important reactions inhibiting reactivity is the concerted elimination reaction: p -, s -C₄H₉O₂ = 1-, 2-C₄H₈ + HO₂.

Acknowledgments

This work was supported primarily by Rolls-Royce Canada Ltd. Partial support for the experiments came from The Aerospace Corporation and The National Science Foundation under grant CBET-0832561. The authors (TAMU) gratefully acknowledge the assistance of Danielle Kalitan, Nolan Polley, Rodrigo Garza, and Sean Baker in performing some of the shock-tube experiments.

Appendix A. Supplementary material

Supplementary data associated with this article can be found, in the online version, at doi:10.1016/j.combustflame.2010.01.016.

References

- [1] G.A. Richards, M.M. McMillian, R.S. Gemmen, W.A. Rogers, S.R. Cully, *Prog. Energy Combust. Sci.* 27 (2001) 141–169.
- [2] T. Lieuwen, V. McDonnell, E. Petersen, D. Santavicca, *J. Eng. Gas Turb. Power* 130 (2008) 11506-1–11506-10.
- [3] N. Donato, C. Aul, E. Petersen, C. Zinner, H. Curran, G. Bourque, in: *Proc. ASME Turbo Expo. GT2009-59673*, 2009.
- [4] M.R. Chandraratna, J.F. Griffiths, *Combust. Flame* 99 (1994) 626–634.
- [5] J. Franck, J.F. Griffiths, W. Nimmo, *Proc. Combust. Inst.* 21 (1986) 447–454.
- [6] M. Carlier, C. Corre, R. Minetti, J.F. Pauwels, M. Ribaucour, L.R. Sochet, *Proc. Combust. Inst.* 23 (1990) 1753–1758.
- [7] R. Minetti, M. Ribaucour, M. Carlier, C. Fittschen, L.R. Sochet, *Combust. Flame* 96 (1994) 201–211.
- [8] R. Minetti, M. Ribaucour, M. Carlier, L.R. Sochet, *Combust. Sci. Technol.* 113–114 (1996) 179–192.
- [9] S. Kojima, T. Suzuoki, *Combust. Flame* 92 (3) (1993) 254–265.
- [10] J.F. Griffiths, P.A. Halford-Maw, D.J. Rose, *Combust. Flame* 95 (1993) 291–306.
- [11] H. Kim, Y. Lim, K. Min, D. Lee, *KSME Int. J.* 16 (8) (2002) 1127–1134.
- [12] A. Burcat, K. Scheller, A. Lifshitz, *Combust. Flame* 16 (1971) 29–33.
- [13] D.C. Horning, D.F. Davidson, R.K. Hanson, *J. Propul. Power* 18 (2) (2002) 363–371.
- [14] T. Ogura, Y. Nagumo, A. Miyoshi, M. Koshi, *Energy Fuels* 21 (2007) 130–135.
- [15] R.R. Baker, R.R. Baldwin, A.R. Fuller, R.W. Walker, *J. Chem. Soc. Faraday Trans. 1* (71) (1975) 736–755.
- [16] R.R. Baker, R.R. Baldwin, A.R. Fuller, R.W. Walker, *J. Chem. Soc. Faraday Trans. 1* (71) (1975) 756–779.
- [17] R.D. Wilk, R.S. Cohen, N.P. Cernansky, *Ind. Eng. Chem. Res.* 34 (1995) 2285–2297.
- [18] C.A. Euker Jr., J.P. Leinroth Jr., *Combust. Flame* 15 (1970) 275–287.
- [19] W.J. Pitz, C.K. Westbrook, W.M. Proscia, F.L. Dryer, *Proc. Combust. Inst.* 20 (1984) 831–843.
- [20] M.L. Vermeersch, T.J. Held, Y. Stein, F.L. Dryer, *SAE Trans.* 100 (4) (1991) 645–661.
- [21] M. Cathonnet, J.C. Boettner, H. James, *Proc. Combust. Inst.* 18 (1981) 903–913.
- [22] A. Chakir, M. Cathonnet, J.C. Boettner, F. Gaillard, *Combust. Sci. Technol.* 65 (1989) 207–230.
- [23] V.K. Proudler, P. Cederbalk, A. Horowitz, K.J. Hughes, M.J. Pilling, *Philos. Trans.: Phys. Sci. Eng.*, vol. 337 (1646), *Chem. Instab., Oscillat. Travel. Waves* 15 (November) (1991) 211–221.
- [24] P. Dagaut, J. Luche, M. Cathonnet, *Energy Fuels* 14 (2000) 712–719.
- [25] W.J. Pitz, C.K. Westbrook, W.R. Leppard, *Society of Automotive Engineers Publication*, SAE-881606, 1988.
- [26] J.R. Smith, R.M. Green, C.K. Westbrook, W.J. Pitz, *Proc. Combust. Inst.* 20 (1984) 91–100.
- [27] R.D. Wilk, R.M. Green, W.J. Pitz, C.K. Westbrook, S. Addagarla, D.L. Miller, N.P. Cernansky, *Society of Automotive Engineers Publication*, SAE-900028, 1990.
- [28] Y. Yamasaki, N. Iida, in: *5th International Symposium on Diagnostics and Modeling of Combustion in Internal Combustion Engines (COMODIA 2001)*, July 1–4, 2001, pp. 417–425.
- [29] Y. Yamasaki, N. Iida, *JSME Int. J.* 26 (1) (2003) 52–59.
- [30] S. Kojima, *Combust. Flame* 99 (1994) 87–136.
- [31] J. Warnatz, *Combust. Sci. Technol.* 34 (1983) 177–200.
- [32] W.J. Pitz, C.K. Westbrook, *Combust. Flame* 63 (1–2) (1986) 113–133.
- [33] R.D. Wilk, W.J. Pitz, C.K. Westbrook, S. Addagarla, D.L. Miller, N.P. Cernansky, R.M. Green, *Proc. Combust. Inst.* 23 (1990) 1047–1056.
- [34] S. Wang, D.L. Miller, N.P. Cernansky, *Society of Automotive Engineers Publication*, SAE-962106, 1996.
- [35] F. Buda, R. Bounaceur, V. Warth, P.A. Glaude, R. Fournet, F. Battin-Leclerc, *Combust. Flame* 142 (2005) 170–186.
- [36] L. Brett, Ph.D. Thesis, National University of Ireland, Galway, 1999.
- [37] L. Brett, J. MacNamara, P. Musch, J.M. Simmie, *Combust. Flame* 124 (2001) 326–329.
- [38] S. Gallagher, H.J. Curran, W.K. Metcalfe, D. Healy, J.M. Simmie, G. Bourque, *Combust. Flame* 153 (2008) 316–333.
- [39] E.L. Petersen, D.M. Kalitan, S. Simmons, G. Bourque, H.J. Curran, J.M. Simmie, *Proc. Combust. Inst.* 31 (2007) 447–454.
- [40] E.L. Petersen, M.J.A. Rickard, M.W. Crofton, E.D. Abbey, M.J. Traum, D.M. Kalitan, *Meas. Sci. Technol.* 16 (2005) 1716–1729.
- [41] D. Healy, H.J. Curran, S. Dooley, J.M. Simmie, D.M. Kalitan, E.L. Petersen, G. Bourque, *Combust. Flame* 155 (2008) 451–461.
- [42] C. Morley, <http://www.arcl02.dsl.pipex.com/gseqrite.htm%3e>.
- [43] C.J. Aul, J. de Vries, E.L. Petersen, Eastern States Fall Technical Meeting of the Combustion Institute, October 21–24, Charlottesville, VA, 2007.
- [44] E.L. Petersen, J.M. Hall, S.D. Smith, J. de Vries, A. Amadio, M.W. Crofton, *J. Eng. Gas Turbines Power* 129 (2007) 937–944.
- [45] M.J.A. Rickard, J.M. Hall, E.L. Petersen, *Proc. Combust. Inst.* 30 (2005) 1915–1923.
- [46] E.L. Petersen, *Combust. Sci. Technol.* 181 (2009) 1123–1144.
- [47] H.J. Curran, P. Gaffuri, W.J. Pitz, C.K. Westbrook, *Combust. Flame* 114 (1998) 149–177.
- [48] H.J. Curran, P. Gaffuri, W.J. Pitz, C.K. Westbrook, *Combust. Flame* 129 (2002) 253–280.
- [49] G. Bourque, D. Healy, H.J. Curran, C. Zinner, D. Kalitan, J. de Vries, C. Aul, E. Petersen, *Proc. ASME Turbo Expo.* 3 (2008) 1051–1066.
- [50] C.M. Lund, L. Chase, HCT – A General Computer Program for Calculating Time-Dependent Phenomena Involving One-dimensional Hydrodynamics, Transport, and Detailed Chemical Kinetics, Lawrence Livermore National Laboratory Report UCRL-52504, Revised, 1995.
- [51] M.A. Oehlschlaeger, D.F. Davidson, R.K. Hanson, *J. Phys. Chem. A* 108 (2004) 4247–4253.
- [52] R.G. Gilbert, K. Luther, J. Troe, Ber. Bunsenges. Phys. Chem. 87 (1983) 169–177.
- [53] J.P. Orme, H.J. Curran, J.M. Simmie, *J. Phys. Chem. A* 110 (2006) 114–131.
- [54] J. Aguilera-Iparraguirre, H.J. Curran, W. Klopper, J.M. Simmie, *J. Phys. Chem. A* 112 (30) (2008) 7047–7054.
- [55] H.-H. Carstensen, A.M. Dean, O. Deutschmann, *Proc. Combust. Inst.* 31 (2007) 149–157.
- [56] H.J. Curran, *Int. J. Chem. Kinet.* 38 (2006) 250–275.
- [57] D.M. Matheu, W.H. Green Jr., J.M. Grenda, *Int. J. Chem. Kinet.* 35 (2003) 95–119.
- [58] J.D. DeSain, S.J. Klippenstein, J.A. Miller, C.A. Taatjes, *J. Phys. Chem. A* 107 (2003) 4415–4427.
- [59] W. Tsang, *J. Phys. Chem. Ref. Data* 20 (1991) 221–273.
- [60] T.A. Barckholtz, J.W. Bozzelli, C. Chen, in: *Proc. Third Joint Meeting US Sections Combustion Institute Paper A42*, University of Illinois at Chicago, March 16–19, 2003.
- [61] C. Naik, Modeling the Low to Intermediate Temperature Oxidation and Pyrolysis of Hydrocarbons Ph.D. Thesis, Chemical Engineering Dept., Colorado School of Mines, USA, 2004.
- [62] C.D. Wijaya, R. Sumathi, W.H. Green Jr., *J. Phys. Chem. A* 107 (2003) 4908–4920.
- [63] C.K. Westbrook, H.J. Curran, W.J. Pitz, J.F. Griffiths, C. Mohamed, S.K. Wo, *Proc. Combust. Inst.* 27 (1998) 371–378.
- [64] S. Gersen, A.V. Mokhov, J.H. Darneveil, H.B. Levinsky, *Combust. Flame* 157 (2010) 240–245.
- [65] E.J. Silke, H.J. Curran, J.M. Simmie, *Proc. Combust. Inst.* 30 (2005) 2639–2647.
- [66] J. Würmel, E.J. Silke, H.J. Curran, M.S. Ó Conaire, J.M. Simmie, *Combust. Flame* 151 (2007) 289–302.
- [67] D. Healy, H.J. Curran, J.M. Simmie, D.M. Kalitan, C.M. Zinner, A.B. Barrett, E.L. Petersen, G. Bourque, *Combust. Flame* 155 (2008) 441–448.
- [68] D.J.M. Ray, R.R. Diaz, D.J. Waddington, *Proc. Combust. Inst.* 14 (1973) 259–266.
- [69] D.J.M. Ray, D.J. Waddington, *Combust. Flame* 20 (1973) 327–334.